Nanoscale

Structure-activity relationship of nanostructured ceria for the catalytic generation of hydroxyl radicals

Journal:	*Nanoscale*
Manuscript ID	NR-ART-11-2018-009393.R1
Article Type:	Paper
Date Submitted by the Author:	31-Jan-2019
Complete List of Authors:	Fisher, Tamra; University of Nebraska-Lincoln, Chemistry Zhou, Yunyun; University of Nebraska-Lincoln, Chemistry Wu, Tai-Sing; National Tsing Hua University, Physics Wang, Meiyu; University of Nebraska-Lincoln Soo, Yun-Liang; National Tsing Hua University; National Synchrotron Radiation Research Centre Cheung, Chin Li; University of Nebraska-Lincoln, Chemistry

Nanoscale

ARTICLE

Structure-activity relationship of nanostructured ceria for the catalytic generation of hydroxyl radicals

Received 00th January 20xx,
Accepted 00th January 20xx

DOI: 10.1039/x0xx00000x

www.rsc.org/

Tamra J. Fisher,[a] Yunyun Zhou,[a,†] Tai-Sing Wu,[b] Meiyu Wang,[c] Yun-Liang Soo,[b, d] and Chin Li Cheung*[, a]

Reactive oxygen species (ROS) are powerful oxidants generated in both biological systems and natural environments. Though enzyme-mimic activity and Fenton-like reactions have been postulated to explain how ceria nanoparticles and ROS involve in the catalytic decomposition of hydrogen peroxide (H_2O_2), the corresponding reaction kinetics for this reaction have yet been completely resolved. Here we present our investigation of the structure-activity relationship of ceria nanostructures for the generation of hydroxyl radicals through the catalytic decomposition of H_2O_2. Different nanostructured ceria including nanorods (NR), nanocubes (NC), and nanooctahedra (NO), together with commercial ceria, were examined to elucidate the relationship between morphology and the reaction kinetics. Initial relative production rates of hydroxyl radicals over different ceria nanostructures were determined using fluorescence measurements and were applied to obtain the apparent activation energy for their intrinsic activity comparisons. The activity trend of order: ceria NR > ceria NC > ceria NO > commercial ceria was observed. This trend was rationalized and assessed using activity descriptive factors including the intensity ratio of Raman bands of vibration modes due to atomic defects, the percentage of surface Ce^{3+} content, and the average coordination number of oxygen anions surrounding each cerium cation in the ceria samples.

Introduction

Cerium oxide (or ceria) is a unique redox catalyst which has been investigated for applications ranging from electrocatalysis and solid oxide fuel cells to organic chemical synthesis. The unique redox activity of ceria originates from its large intrinsic storage and release capacity of oxygen. This capacity is associated with the formation of oxygen vacancy defects (OVDs) and the low potential redox transformation between Ce^{3+} and Ce^{4+}.[1, 2] The surface and subsurface OVDs and subsequent Ce^{3+} have been postulated to be active sites for catalysis because reactants are considered to directly interact with the exposed Ce^{3+}. Due to these properties, ceria has been shown to be excellent oxidizing and reducing agents. Consequently, the shape and facet effects on ceria's catalytic performance have recently attracted interests for various reactions.[3-6]

Reactive oxygen species (ROS) are a category of natural products from oxygen metabolism.[7] Typical examples of ROS include hydrogen peroxide (H_2O_2), singlet oxygen ($^1O_2$), superoxides (O_2^-), hydroxyl radicals (•OH), and hydroperoxyl radicals (•OOH). They play essential roles in natural and biological environments due to their high oxidizing power. For example, cell signaling and homeostasis are processes critical to functionalities which require certain levels of ROS.[7-9] In order to maintain this finite balance, ROS are constantly being generated and eliminated in biological systems. Environmental stress can disrupt this balance, resulting in extreme concentrations of ROS. Excessive ROS can cause cell death and has been linked to diseases such as cancer and brain dysfunction.[10, 11] Therapeutic studies have investigated controlled generation and remediation of ROS for treatment purposes.[12, 13] The significance of controlled ROS generation is not limited to health and medicine. Intentional generation of ROS has provided highly clean and efficient water treatment methods.[14, 15] For example, studies have shown that •OH can completely oxidize non-biodegradable organic compounds in contaminated surface water to CO_2 and H_2O.[15] Their uses have also been extended to antibacterial treatment and food preservation.[16-18]

Ceria has been postulated to generate and mitigate ROS through different redox reaction pathways including enzyme-mimic activities and Fenton-like reactions.[14, 19, 20] The majority of these reported investigations have focused on the scavenging properties. For example, for the ceria-catalyzed decomposition and scavenging of H_2O_2, a superoxide dismutase-mimic (SOD-mimic) property was hypothesized to explain how ceria nanoparticles scavenge O_2^-, whereas a catalase-mimic activity was proposed to generate H_2O_2 upon the increasing concentration of Ce^{4+} in these particles.[21, 22] The

[a] Department of Chemistry, University of Nebraska-Lincoln, Lincoln, Nebraska 68588, United States
[b] Department of Physics, National Tsing Hua University, Hsinchu 30013, Taiwan, R.O.C.
[c] Department of Mechanical and Materials Engineering, University of Nebraska-Lincoln, Lincoln, Nebraska 68588, United States
[d] National Synchrotron Radiation Research Centre, Hsinchu 30076, Taiwan, R.O.C.
† Present Address: National Energy Technology Laboratory, Pittsburgh, PA, 15236, United States
* Corresponding Author. Dr. Chin Li Cheung; Email: ccheung2@unl.edu
Electronic Supplementary Information (ESI) available: additional characterization of ceria samples, XPS data, kinetics data, and negative controls for reactions. See DOI: 10.1039/x0xx00000x

corresponding reactions are often reported as follows:

SOD-mimic reaction:

$$O_2^- + Ce^{3+} + 2H^+ \rightarrow H_2O_2 + Ce^{4+} \quad (1)$$

Catalase-mimic reaction:

$$H_2O_2 + 2Ce^{4+} \rightarrow O_2 + 2H^+ + 2Ce^{3+} \quad (2)$$

Nonetheless, these proposed enzyme-mimic pathways do not consider the involvement of other ROS species (such as •OH) which have also been identified to be present during the catalytic decomposition of H_2O_2.

The generation of ROS through decomposition of hydrogen peroxide (H_2O_2) has also been accepted to follow Fenton or Fenton-like reactions when reducible metal ions such as iron (II), copper (I), and chromium (III) ions are present.[15, 23, 24] Using iron (II) ions as an example, the first steps of Fenton reactions under acidic, neutral, and alkaline conditions are as follows:

Under acidic conditions:

$$Fe^{2+} + H_2O_2 + H^+ \rightarrow Fe^{3+} + \bullet OH + H_2O \quad (3)$$

Under neutral and alkaline conditions:

$$Fe^{2+} + H_2O_2 \rightarrow Fe^{3+} + \bullet OH + OH^- \rightarrow Fe(OH)_2^+ + \bullet OH \quad (4)$$

Other catalysts including reducible transition metals oxides such as titanium oxide and doped-metal oxides may also follow Fenton-like reactions.[25, 26] For all these catalysts, the multiple oxidation states of the metal ions in these catalysts allow them to act as both electron donors and acceptors in radical generation reactions.

In addition to the multiple proposed pathways, the roles of ceria catalysts in reduction-oxidation reactions have been found to vary according to the synthetic and reaction conditions.[27, 28] As such, additional experimentation is necessary to resolve the reaction mechanism.[29, 30] While different reaction mechanisms and active sites have been proposed, most attribute the catalytic activity to the presence of coexisting Ce^{3+}/Ce^{4+} valence states or the presence of oxygen vacancy defects (OVDs).[7, 19, 31-34] To our best knowledge, the relationships between ceria catalysts with facet-dependent morphology and their catalytic activity towards the decomposition of H_2O_2 and consequent generation of ROS have not been reported.

Herein we present our study of the structure-activity relationship of ceria nanostructures for the generation of hydroxyl radicals (•OH) through the catalytic decomposition of hydrogen peroxide (H_2O_2) under low concentration conditions. The catalytic activities of different nanostructured ceria including nanorods (NR), nanocubes (NC), and nanooctahedra (NO), together with commercial ceria, were examined to elucidate the relationship between morphology and the reaction kinetics. Initial relative production rates of hydroxyl radicals over these different ceria nanostructures at different reaction temperatures were measured using a dye-based fluorescence method. The temperature-dependent rate data were used to construct Arrhenius plots for obtaining the apparent activation energy for comparing the intrinsic activities of these catalysts. In addition, activity descriptive factors including the intensity ratio of Raman bands of vibration modes due to atomic defects, the percentage of surface Ce^{3+} content, and the average coordination number of oxygen anions surrounding each cerium ion in the ceria samples were assessed for examining their roles in the structure-activity relationship.

Experimental

Synthesis of nanostructured ceria

Ceria nanorods (NR), nanocubes (NC), and nanooctahedra (NO) were synthesized using hydrothermal methods adapted from previous literature.[35] Briefly, to synthesize ceria NR, 2 mmol of cerium (III) nitrate hexahydrate ($Ce(NO_3)_3{\cdot}6\,H_2O$, 99.99 %, Alfa Aesar, Tewksbury, MA) were suspended in 40 mL of 10 M aqueous sodium hydroxide (NaOH, 99.95%, Sigma-Aldrich, St. Louis, MO) solution and were then heated to 120 °C for 15 h. in a Teflon-lined stainless steel autoclave (Parr Instruments, Moline, IL). To produce ceria NC, 8 mmol of $Ce(NO_3)_3{\cdot}6\,H_2O$ and 1 mol. of NaOH pellets were stirred in 160 mL of Nanopure water (18 MΩ·cm deionized water from Synergy filtration system (VWR, Randor, PA)) for 30 min. The resulting purple slurry was transferred to four 45-mL Teflon-lined stainless steel autoclaves and heated to 180 °C for 24 h. Ceria NO were synthesized by preparing a suspension of 8 mmol of $Ce(NO_3)_3{\cdot}6\,H_2O$ and 0.08 mmol of sodium phosphate dodecahydrate ($Na_3PO_4{\cdot}12\,H_2O$, ≥ 98.0%, Sigma-Aldrich, St. Louis, MO) in 320 mL of Nanopure water. After being stirred for 1 h., the mixture was subsequently transferred to the autoclaves in 40 mL aliquots and heated to 170 °C for 6 h. The hydrothermal product was composed of largely NO with some NR impurities. This product was further treated with a solution of nitric acid, hydrochloric acid, and Nanopure water (ratio: 1:3:2) for 1 h. to selectively dissolve NR. The resulting products were washed with Nanopure water, leaving only the NO product. All ceria products from the autoclaves were filtered with 0.2-micron pore-etched polycarbonate membranes (Millipore, Burlington, MA), washed with Nanopure water, and dried in a convection oven at 50 °C overnight. Commercial ceria (average size of 80 nm, 99.9% by metal basis) from Alfa Aesar was used for catalytic activity and structure comparison studies (Figure S1). All ceria samples were annealed at 400 °C, in a flow of 200 SCCM of simulated air (N_2: O_2 = 8:2, Matheson Trigas, Basking Ridge, NJ), and under 2 Torr for 30 min. before use.

Characterization of ceria samples

The lattice structures and morphology of the different ceria samples were investigated using powder X-ray diffraction (XRD), Raman spectroscopy, and transmission electron microscopy (TEM). Powder XRD patterns of ceria samples were obtained using a PANalytical Empyrean diffractometer (PANalytical, Inc., Westborough, MA) with a Cu Kα X-ray source of an average wavelength of 1.544 Å. UV-Raman spectra of ceria samples were collected on a Horiba LabRam HR Evolution Raman spectrometer (Horiba Jobin Yvon, Edison, NJ) with a 364 nm laser. TEM images of the samples were collected on an FEI Tecnai Osiris S/TEM (FEI, Hillsboro, Oregon) operated at 200 kV.

The percentages (%) of Ce^{3+} content at the surfaces of ceria samples were determined using X-ray photoelectron spectroscopy (XPS) performed on a Thermo Scientific K-alpha+ X-ray photoelectron spectrometer system (Thermo Fisher Scientific, LLC, Waltham, MA) equipped with monochromatic Al Kα X-ray (1486.6 eV). The photoelectrons were collected at 55° emission angle. The kinetic energy of photoelectrons was determined using a hemispherical analyzer in the constant

analyzer energy mode with 200 eV pass energy for survey spectra and 50 eV pass energy for high resolution spectra of elements. An argon ion flood gun was used for automatic charge neutralization of the samples. Carbon 1s peak at 284.6 eV was used for the calibration of the XPS data. The Ce 3d XPS spectra were analyzed using a published quantitative method[36] to obtain the % of surface Ce^{3+} content information.

The local atomic structures were studied using the extended X-ray-absorption fine structure (EXAFS) technique. Measurements of the Ce L_3-edge EXAFS spectra were performed at the beamline BL17C of the Taiwan light source at National Synchrotron Radiation Research Center (NSRRC) in Taiwan. The resolution of the energy (ΔE/E) for the incident X-ray photons was estimated to be 2×10^{-4}. The EXAFS spectra of the ceria samples were obtained in the transmission mode using a set of gas ionization chambers. The IFEFFIT software package was employed to examine the EXAFS data for obtaining the local structural parameters of ceria.[37] The fitting parameters for modeling the EXAFS data were constrained by several criteria to exclude unphysical results. The bond lengths of the first Ce-Ce shell and the second Ce-O shell were fixed as the theoretical values, while the energy shifts (ΔE) that largely depended on the atomic species for the first and second O shells were set to be the same.

Kinetics measurements of hydroxyl radical (•OH) generation

Ceria catalysts were used to generate hydroxyl radicals (•OH) by catalytically decomposing hydrogen peroxide (H_2O_2). 3-Aminophenyl fluorescein (APF, Thermo Fisher Scientific, Waltham, MA) was applied in the reaction mixture to detect the presence of •OH produced. APF was chosen because it reacts chemoselectively with •OH to yield fluorescein, which fluoresces at 515 nm. The relative production rates of •OH in these reactions were measured by determining the rates of the increase (or slopes) in the intensity plots of fluorescence signals from fluorescein as a function of time at different reaction temperatures (15 °C to 35 °C). Arrhenius plots of these rate data were then applied to estimate the apparent activation energy values for the catalytic generation of •OH. A range of catalysts (0.1 to 1.0 g/L) and H_2O_2 (0.1 to 6 mM) concentrations was evaluated to establish the structure-activity relationship for each ceria sample. Tris(hydroxymethyl)aminomethane (TRIS, Avantor, Center Valley, PA) and Nanopure water were used to prepare buffered reactant solutions for the reaction. The pH of these solutions was adjusted to pH = 7.4 with concentrated hydrochloric acid. Experimental details for each of the rate measurements were similar. For example, for the kinetic measurement of a reaction mixture containing 3 mM H_2O_2 and 0.1 g/L ceria, 3 mg ceria catalyst was first suspended in 15 mL of 0.1 M TRIS buffer (pH = 7.4). 1.5 mL aliquot of the catalyst stock solution was added to an FUV quartz cell, followed by consecutive additions of 600 µL of 0.1 M TRIS buffer, 900 µL of 10 mM H_2O_2 stock (prepared from 30% H_2O_2 and diluted with 0.1 M TRIS buffer), and 30 µL of 1 mM APF dye. The final concentrations of chemicals in the cell were 0.1 g/L ceria, 3 mM H_2O_2, and 10 µM APF, respectively. To maintain a uniform suspension of ceria catalyst, the reaction mixture was stirred with a stir bar at *ca.* 330 RPM. Kinetics mode on a FluoroMax-4 (Horiba Jobin Yvon, Edison, NJ) was used to measure the emission at 515 nm with excitation at 490 nm at intervals of 30 sec. for a total of 10 min. The temperature of the cell was maintained using a circulating temperature bath connected to the cell holder. To verify that neither ceria catalysts nor unreacted APF were contributing to the observed fluorescence signal, control experiments were performed with each component systematically excluded from the reaction mixture. Negative control experiments were also carried out with the addition of *t*-butyl alcohol, which has been reported to effectively scavenge hydroxyl radicals.[38]

Results and discussion

Structure characterization of ceria samples

The three synthesized ceria samples exhibited three uniquely faceted ceria nanostructures: nanorods (NR), nanocubes (NC), and nanooctahedra (NO) as shown in their TEM images (Figure 1). Commercial bulk ceria used for comparisons was observed to be of faceted particle morphology (Figure S1). Powder XRD patterns of all ceria samples matched that of fluorite-like structured (Fm-3m) cerium (IV) oxide (CeO_2) when compared against the ICCD card # 04-013-4361 (Figure 2). The sharp peaks of these XRD patterns indicated that these ceria samples were highly crystalline. According to the literature used for the syntheses of these ceria structures, excluding the edges, ceria nanorods (NR) display {100} and {111} side facets, whereas ceria nanocubes (NC) possess {100}[39] facets and ceria nanooctahedra (NO) present {111} facets.[40] Since {111} facets were the most stable family of low index facets for ceria and commercial ceria were often synthesized using very high temperature, it was expected that commercial ceria displayed predominantly {111} facets. High resolution TEM images further support the presence of these facets of our ceria samples (Figure 1d, 1e, and 1f). Comparisons of the BET surface area measurements showed that the nanorods possessed the largest surface area among the ceria samples (Table 1). This was not surprising because they were more loosely packed due to their rod morphology and hence had a larger exposed surface area per gram of sample.

Our Raman study revealed that the spectra of all ceria samples display their most intense peaks in the range of 460 to 466 cm^{-1}. This peak is attributed to the F_{2g} vibration mode of fluorite-structured cerium oxide. The locations of this F_{2g} peaks for all three ceria nanostructures are red shifted from that of the commercial ceria (466 cm^{-1}) (Figure 3). Nanorods possess the most significant shift to 460 cm^{-1}. Y. Lee *et al*. attributed this shift to the nanosize of the crystallites and an increase in oxygen vacancy defects (OVDs). In addition, the peak centered around 590 cm^{-1} is attributed to lattice oxygen vacancy defects or the D mode.[32, 41] The broadening of this peak reflects an increase in atomic disorder within the CeO_2 crystal structure of the nanorods.[32, 41] Overbury *et al.* have shown the ratio between the intensity values of these two peaks (I_D/ $I_{F_{2g}}$) to be positively correlated with the density of intrinsic OVD sites. The values of

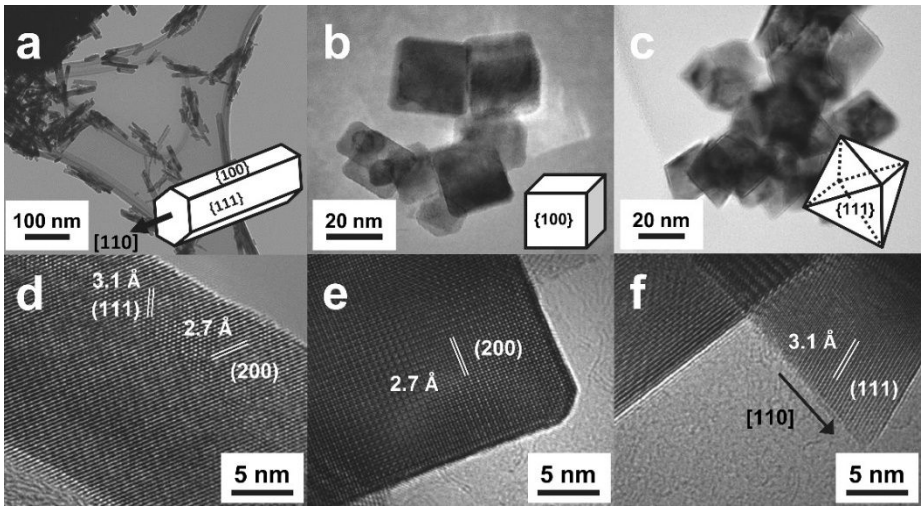

Figure 1. TEM images of ceria nanostructured catalysts: (a) nanorods, (b) nanocubes, and (c) nanooctahedra. Figures (d –f) are the corresponding high-resolution zoom-in images directly below each of the nanostructured ceria.

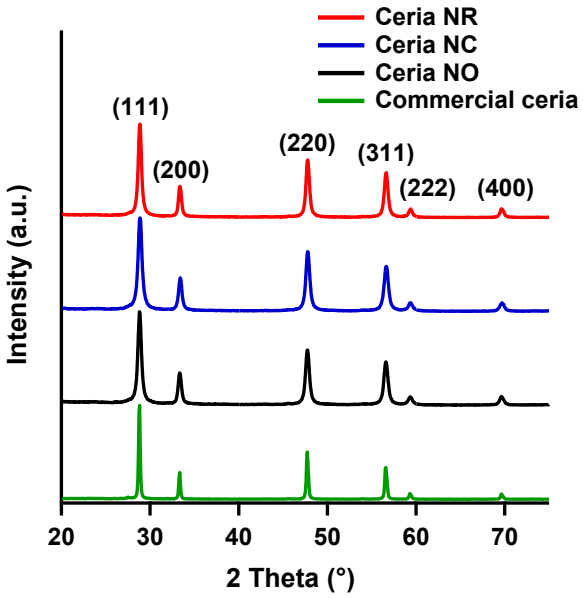

Figure 2. Powder XRD patterns of ceria catalysts: ceria nanorods (NR), ceria nanocubes (NC), ceria nanooctahedra (NO), and commercial ceria. The data was normalized with respect to the (111) peak.

Catalysts	Surface area (m^2/g)	Raman shift of F_{2g} peak (cm^{-1})	$I_D/ I_{F_{2g}}$ ratio
Ceria NR	56	460	1.5
Ceria NC	33	463	0.8
Ceria NO	18	464	0.4
Commercial ceria	5	466	0.05

Table 1. Physical and chemical properties of ceria catalysts.

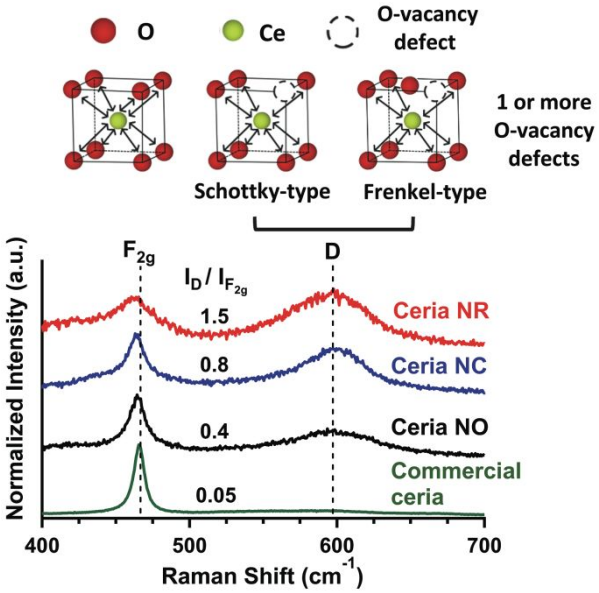

Figure 3. UV-Raman spectra of ceria catalysts. The data were normalized to the F_{2g} peak and shifted upward for display. The values of $I_d/ I_{F_{2g}}$ for each sample were calculated after baseline fittings.

$I_D/ I_{F_{2g}}$ for our structures are in the order: ceria NR (1.5) > ceria NC (0.8) > ceria NO (0.4) >> commercial ceria (0.05), indicating that the nanorods have the most intrinsic OVD sites whereas the commercial ceria has the least. Due to the strong absorption of UV light by the ceria samples, it can thereby be concluded that these defect sites probably primarily populate at the surface and sub-surface regions.[42]

Both Schottky-type[42] and Frenkel-type[32] oxygen vacancy defects have been proposed for the D band assignment in the Raman spectra of ceria. Schottky-type defects refer to point defects composed of vacant cation and anion sites in a stoichiometric ratio. As each oxygen in the stoichiometric fluorite-structured CeO_2 lattice is typically assumed as an anion with a -2 charge, to maintain the charge balance, removing an oxygen anion in the lattice would require substituting two Ce^{4+} ions with two Ce^{3+} ions. This pathway to create a MO_8-type complex oxygen vacancy defect can be expressed using the Kröger–Vink notation: $\emptyset = 2Ce''_{Ce} + V''_O$. For Frenkel-type oxygen vacancy defects, the oxygen anions are displaced from their lattice positions to interstitial sites. These dislocations consequently create vacancies at the original lattice sites.

Our Ce 3d XPS data reveals that the percentages (%) of Ce^{3+} (= $[Ce^{3+}]/ ([Ce^{3+}] + [Ce^{4+}]) \times 100\%$) in the surface and sub-surface regions of the ceria samples are from 15.5% to 18.3%, with a trend order: ceria NR (18.3%) > ceria NC (17.6%) > commercial ceria (16.5%) > ceria NO (15.5%) (Table 1 and Figure S2). The existence of Ce^{3+} cations confirms the likely presence of Schottky-type surface oxygen vacancy defects. Though the trend order for the % of surface Ce^{3+} in general follows that of the $I_D/ I_{F_{2g}}$ Raman data, the differences between the XPS spectra and the analysed Ce^{3+} content between the samples are insignificantly small and thus are insufficient to explain the large differences between the $I_D/ I_{F_{2g}}$ ratios of the ceria samples (Figure S2). As Frenkel-type defects can be created while maintaining a balanced charge ratio in the lattice, similar to the interpretation of ceria nanostructure lattice by Overbury *et al*,[42] we also propose that the $I_D/ I_{F_{2g}}$ ratio of the Raman data indicates largely the presence of Frenkel-type oxygen vacancy defects. Therefore, both Raman and XPS findings suggest that the ceria nanorods should exhibit more "active" surface Ce^{3+} sites and thus are expected to be more catalytically active.

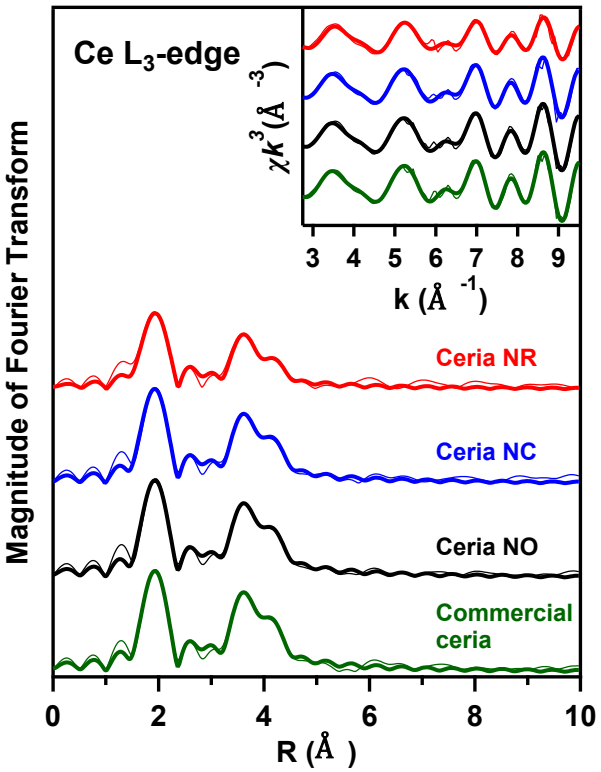

Figure 4. Fourier transformed Ce L_3-edge EXAFS data of ceria catalysts: nanorods (NR), nanocubes (NC), nanooctahedra (NO), and commercial. The inset shows the corresponding EXAFS spectra in *k*-space. Data: thin lines; fittings: thick lines.

Table 2. Fitted structural parameters of the Ce L_3-edge EXAFS analysis for ceria catalysts: nanorods (NR), nanocubes (NC), nanooctahedra (NO), and commercial. *N* is the average coordination number of oxygen anions around the central Ce cations. *R* is the average bond distance. σ^2 is the Debye–Waller factor. Underline marks indicate fixed parameters in the fitting analysis. The ΔE_0 values of two Ce-O shells are constrained to share the same value in the fitting models.

Local structures of the ceria catalysts were also investigated by analysing the Fourier transformed Ce L_3-edge EXAFS spectra (Figure 4). Fittings of the Ce L_3-edge EXAFS for each of the studied catalysts determined the average coordination number of atoms around central Ce atoms (*N*), the average interatomic distance (*R*), and the Debye-Waller factor (σ^2) (Table 2). The ΔE_0 values of two Ce-O shells are constrained to share the same value in the fitting models. Compared with the commercial ceria, all studied ceria nanostructures showed a decrease in coordination of oxygens surrounding the cerium(*N*) in the first Ce-O shell, with a trend of *N*(NR) (6.7 ± 0.5) < *N*(NO) (7.2 ± 0.3) ≈ *N*(NC) (7.3 ± 0.4) < *N*(commercial) (8.0 ± 0.4). As the decrease in Ce-O coordination indicates an increase in the oxygen vacancy in the material, this trend provides the evidence for the significant increase in atomic disorder and presence of OVDs in the nanorods as compared to those of the nanocubes and

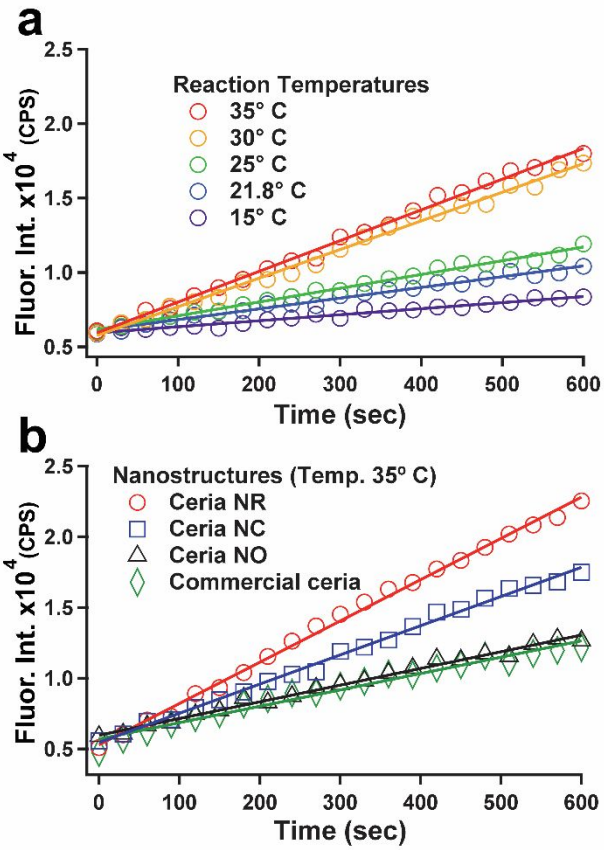

Sample	Atom	*N*	*R* (Å)	σ^2 (10^{-3}Å^2)	ΔE_0 (eV)
Ceria NR	O	6.7 ± 0.5	2.33 ± 0.01	5.7 ± 0.9	8.8 ± 0.5
	Ce	9.5 ± 0.4	3.83	5.3 ± 0.4	4.1 ± 0.3
	O	12.6 ± 1.4	4.49	5.6 ± 1.3	8.8 ± 0.5
Ceria NC	O	7.3 ± 0.4	2.33 ± 0.01	3.6 ± 0.7	7.3 ± 0.3
	Ce	10.1 ± 0.3	3.83	4.0 ± 0.3	3.0 ± 0.3
	O	14.7 ± 1.0	4.49	2.0 ± 0.7	7.3 ± 0.3
Ceria NO	O	7.2 ± 0.3	2.33 ± 0.01	3.2 ± 0.6	7.5 ± 0.3
	Ce	9.8 ± 0.3	3.83	2.9 ± 0.2	3.2 ± 0.2
	O	15.8 ± 1.0	4.49	3.0 ± 0.7	7.5 ± 0.3
Commercial	O	8.0 ± 0.4	2.34 ± 0.01	4.1 ± 0.8	7.7 ± 0.4
ceria	Ce	11.2 ± 0.3	3.83	3.1 ± 0.3	3.7 ± 0.2
	O	19.3 ± 1.3	4.49	5.1 ± 0.8	7.7 ± 0.4

nanooctahedra as well as the commercial ceria. Note that compared to other ceria samples, the larger decrease in the coordination numbers for the second Ce-Ce shell and the third Ce-O shell of the ceria nanorods further corroborated the larger degree of atomic disorder in ceria nanorods. Though a report on the modeling of oxygen vacancy defects in ceria has predicted a decrease in the average Ce-O bond length due to the anisotropic chemical strain in the lattice,[39] such a decrease is very modest among our nanostructured ceria samples examined in this study (2.33 ± 0.01 Å) when compared to that of the commercial sample (2.34 ± 0.01 Å).

Kinetics of hydroxyl radical (•OH) generation using ceria catalysts

In general, mixtures of 30% hydrogen peroxide aqueous solutions and ceria catalysts were observed to yield bubbles of oxygen at room temperature. However, the evolution of oxygen bubbles ceased to be observable by eye in control experiments without ceria. The catalytic effect of ceria on the decomposition of H_2O_2 is proposed to follow Fenton-like reactions, with •OH reportedly being the first ROS generated by this process.[43] This is similar to the case of the Fenton reaction using iron(II) ions to catalyze the disproportionation of H_2O_2 under neutral and alkaline conditions as expressed by the equation: $Ce^{3+} + H_2O_2 \rightarrow Ce^{4+} + \bullet OH + OH^-$.

To selectively study the kinetics for the generation of hydroxyl radicals (•OH) from the ceria-catalyzed decomposition of H_2O_2, we applied the chemoselective APF dye to the reaction mixture and measured the relative production rate of •OH in the reaction.[44-46] APF is a non-fluorescent molecule. Typically, after APF molecules react with hydroxyl radicals, peroxynitrate anions, or hypochlorite anions, the resulting products exhibit bright green fluorescence with excitation/emission maxima of 490/515 nm. Considering the chemical species present in our reaction mixture, only •OH has the potential to react with APF.

By measuring the slopes of the fluorescence intensity versus reaction time plots, we obtained the relative apparent reaction rates (k) for the generation of •OH with different ceria nanostructures under low concentration of H_2O_2 (3 mM). For example, Figure 5a shows the fluorescence signals detected as a function of reaction time for experiments catalyzed by ceria nanorods at different reactions temperatures (15 °C – 35 °C). As the reaction temperature increased, the relative apparent reaction rates (or the slope of the plots) increased.

We expect that •OH detected in our kinetics measurements are mainly from Fenton-like reaction pathways, not from other ROS reactions with H_2O_2. In our previous work on catalytic decomposition of H_2O_2 by ceria nanorods, our *in situ* EXAFS study established the redox cycling of cerium which suggest the decomposition reaction follows a Fenton-like reaction pathway.[43] Since APF chemoselectively scavenged •OH generated from the H_2O_2 decomposition reaction, other follow-up reactions dependent on the availability of •OH were effectively prevented. For example, the Haber-Weiss reaction necessitates the presence of additional radicals like O_2^- to produce •OH, but O_2^- are needed to be first generated from the reaction of •OH and H_2O_2.

Figure 5. Reaction kinetics of the catalytic generation of hydroxyl radicals from hydrogen peroxide over ceria catalysts. (a) Plots of fluorescence intensity vs. reaction time for ceria nanorods at different reaction temperatures (15, 21.8, 25, 30, and 35 °C). (b) Plots of fluorescence intensity vs. reaction time for four different ceria catalysts at 35 °C. Reaction conditions: [H_2O_2] = 3 mM; [Ceria NR] = 0.1 g/L.

To further confirm that only •OH reacted with the dye, we performed additional negative control experiments by adding *t*-butanol, which is a known •OH scavenger, to the reaction mixture.[38, 47] This negative control showed that, when compared to the background signal, no appreciable changes were observed in the fluorescence intensity of the reaction mixture over a 10 min.-long reaction, evidencing that other species capable of reacting with APF were absent (Figure S3).

The effects of different concentrations of H_2O_2 and ceria on the catalytic reaction kinetics were investigated using the ceria nanorods by measuring the changes in the relative reaction rates (Figures S4 and S5). As the concentration of H_2O_2 increased from 0.1 to 6 mM, the reaction order with respect to H_2O_2 was determined to decrease from 0.74 to *ca.* 0. The chosen concentration of 3 mM H_2O_2 for the comparison of catalyst activity falls within a distinct plateau region in the plot of initial reaction rate vs. $[H_2O_2]$. This indicates that the measured apparent reaction rate data was primarily affected by the properties of the ceria catalyst rather than the concentration of H_2O_2. Similarly, the effects of ceria concentration from 0.1 – 1.0 g/L were also investigated. The reaction order with respect to catalyst concentration was also determined to be close to 1 (0.89). This result indicates that the concentration of catalyst was sufficiently high and there was no considerable effect due to mass transport limitations.[48]

Ideally, one would apply the relative apparent reaction rates to infer the intrinsic catalytic activity of different ceria catalysts. Such comparisons could be misleading because the rate differences could also be influenced by extrinsic factors including differences in the catalysts' surface areas and their density of catalytically active surface sites. Reported literature primarily resorts to normalizing the reaction kinetics data by the BET surface areas of catalysts or their weight for comparing the activity of different catalysts. For example, Figure 5b illustrates the apparent reaction rates for the decomposition of H_2O_2 with ceria nanorods, ceria nanocubes and ceria nanooctahedra at the reaction temperature of 35 °C. The activity trend according to the relative rates appears to be in the order: ceria NR > ceria NC > ceria NO ≈ commercial ceria. This trend roughly follows the trend of BET surface areas of these samples. However, comparisons of surface-area normalized relative reaction rates would suggest the (111) faceted commercial ceria as the most active ceria catalyst (data not shown), which contradicts many literature reports (such as *Wang et al.*[35]) that ceria nanorods are more catalytically active than (111) faceted ceria catalysts. In addition, surface-area normalization does not account for differences in the density and types of OVDs indicated by Raman, XPS, and EXAFS analysis. The differences in the density and types of point defects may also affect the likelihood of defect clustering[49] which could lead to higher intrinsic activity. To avoid complications in comparisons due to the differences in extrinsic factors between the samples, we instead applied the measured temperature-dependent apparent reaction rates to construct Arrhenius plots and thereby determined the apparent activation energy values (E_a) for each of the studied catalyst morphologies (Figure 6). As the production of •OH is postulated to be rate-determining, the apparent activation energy barrier can be determined from the fluorescence studies and be used to directly compare the catalytic activity of various ceria nanostructures. The logarithmic relationships in the Arrhenius plots negate the necessity of normalizing fluorescence signals between samples to account for extrinsic differences in aspects such as surface area per gram to provide accurate, intrinsic catalytic efficiency comparisons. From these Arrhenius plots, we determined the apparent activation energy values for ceria NR, NC, NO, and commercial ceria to be 46±2, 50±2, 61±3, and 70±11 kJ/mol, respectively (Table 1). The large error associated with commercial ceria resulted from its low activity and low observed fluorescence signal compared to the background noise. Coincidentally, the activity trend (ceria NR > ceria NC > ceria NO > commercial ceria) follows a similar trend as the apparent rate comparison in Figure 5.

Structure-activity relationship for hydroxyl radical (•OH) generation using ceria catalysts

The degrees of intrinsic defects in the atomic structures of the examined ceria nanostructures were found positively associated with the differences in the observed activity. Each of the studied ceria morphologies exhibits differences in disorder and density of OVDs, following the trend: ceria NR > ceria NC > ceria NO > commercial ceria. This positively correlates to the activity trend (ceria NR > ceria NC > ceria NO > commercial ceria). We note that the activity trend (ceria NR > ceria NC > ceria NO > commercial ceria) established by the measured apparent activation energy mirrors well with the observed

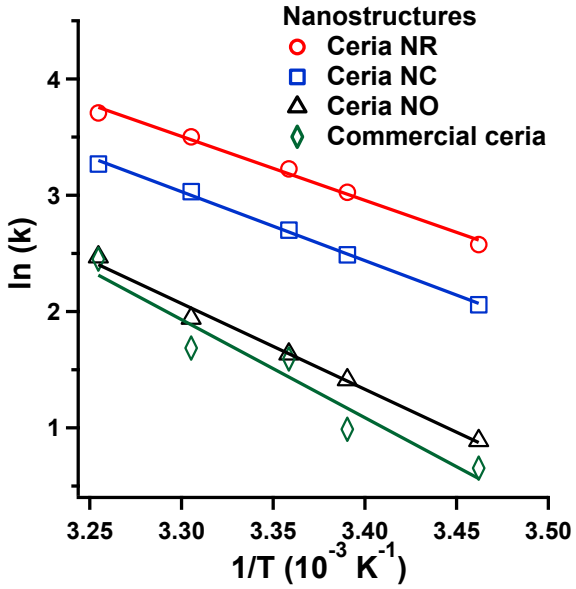

Figure 6. Arrhenius plots for the reaction kinetics of catalytic generation of hydroxyl radicals over ceria catalysts. Reaction conditions: $[H_2O_2]$ = 3 mM; [Ceria catalyst] = 0.1 g/L.

differences in the peak intensity ratios of the Raman D and F_{2g} peaks (I_D/ $I_{F_{2g}}$) that largely indicate higher surface and sub-surface Frenkel-type OVD density of the studied ceria samples (Table 1). The activity trend also corroborates well with the decrease in the average coordination number of oxygens surrounding cerium, which indicates higher disorder and

increased oxygen vacancy defects in the ceria catalysts. Nonetheless, since the percentages of surface Ce^{3+} content of examined ceria catalysts are very similar, this factor which reveals the density of Schottky-type oxygen vacancy defects has an insignificant correlation to our observed activity trend for our studied reaction.

Among the studied nanostructures, nanorods were found to possess the greatest surface and sub-surface Schottky-type and Frenkel-type OVDs. High OVD density is often reported to be correlated with exposed Ce^{3+} catalytic sites and increased intrinsic catalytic activity.[31-34] This is consistent with the observed activity trend. While the detailed reaction kinetics are yet reported, it is generally accepted that generation of •OH is the rate-determining step and the electron transfer from a metal ion is necessary to produce •OH. Thus, ceria facets with higher density of surface and sub-surface OVDs are expected to be more catalytic active.

The morphologies of ceria catalysts studied displayed unique facets with varying density and accessibility of Ce^{3+} and OVDs. If edges are not considered, ceria nanorods display {100} and {111} side facets and {110} end facets, whereas nanocubes possess primarily {100} facets and nanooctahedra present mainly {111} facets. In this study, ceria nanorods exhibited the highest activity and lowest apparent activation energy barrier as well as highest OVD density. The catalytic activity trend further correlated well to the surface and sub-surface OVD population for the other morphologies studied. Considering that the activity for the decomposition of H_2O_2 was positively correlated to the density of OVDs and the reactivity of OVDs are related to the exposed facets, the observed trend can be extended to correlate the activity trend to the facets.[32] Thus, {100} facets are concluded to be more active than {111} facets for our studied reaction.

Metal catalysts such as palladium are considered to be the standard catalyst for studying H_2O_2 decomposition due to their high activity and low apparent activation energy barrier (53±3 kJ/mol).[50-52] Comparatively, our ceria nanorods demonstrate an apparent energy barrier of 46±2 kJ/mol. Even though the palladium catalytic site density of is much higher than that of cerium oxide, our demonstrated fluorescent method has shown sensitivity sufficient to discern the intrinsic catalytic activity of ceria with varying density of catalytic sites.

Conclusions

In summary, ceria nanostructures exhibiting morphologies of nanorods, nanocubes, and nanooctahedra were studied for the catalytic generation of •OH from the decomposition of H_2O_2. An activity trend of ceria NR > ceria NC > ceria NO > commercial ceria was observed. Both the atomic disorder determined by EXAFS and the intensity ratio of Raman bands of vibration modes (I_D/ $I_{F_{2g}}$) that infers the densities of surface and sub-surface oxygen vacancy defects in ceria were found to be pragmatic activity descriptive factors to predict this activity trend for our studied reaction. While the percentage of surface Ce^{3+} content from the XPS analysis also indicates a similar trend, the small differences between the corresponding values of the examined ceria samples suggest that this activity descriptive factor is less indicative to differentiate the intrinsic activities of ceria catalysts in our study. This is probably because the Frenkel-type OVDs revealed by the Raman data are more catalytically active for our studied reaction than the Schottky-type OVDs indicated by the % of surface Ce^{3+}. Our analysis of the structure-activity relationships has led to our proposition that the activity trend is largely dependent on the types and density of surface and sub-surface OVDs, which change with the nanostructured morphology. These findings and our demonstrated fluorescence method are expected to be practical for evaluating the catalytic activity of ceria of different morphologies and studying their ROS scavenging capability in biological and non-biological systems where controlled decomposition of H_2O_2 and generation of •OH are of critical concerns.[19, 29, 53]

Conflicts of interest

The authors have no conflicts to declare.

Acknowledgements

The authors thank the financial support from the National Science Foundation (CHE-1362916). The research was performed in part in the Nebraska Nanoscale Facility: National Nanotechnology Coordinated Infrastructure and the Nebraska Center for Materials and Nanoscience (NCMN) supported by the National Science Foundation under Award ECCS-1542182, and the Nebraska Research Initiative. We acknowledge the National Radiation Research Center in Taiwan for the use of their synchrotron light source. We are also grateful to Max Wetherington from the Penn State for the Raman data collection and Bala Balasubramanian from NCMN for the XPS data collection.

Notes and references

1. N. J. Lawrence, J. R. Brewer, L. Wang, T.-S. Wu, J. Wells-Kingsbury, M. M. Ihrig, G. Wang, Y.-L. Soo, W.-N. Mei and C. L. Cheung, *Nano Lett.*, 2011, **11**, 2666-2671.
2. F. Esch, S. Fabris, L. Zhou, T. Montini, C. Africh, P. Fornasiero, G. Comelli and R. Rosei, *Science*, 2005, **309**, 752-755.
3. C. Zang, X. Zhang, S. Hu and F. Chen, *Appl. Catal. B*, 2017, **216**, 106-113.
4. J. Han, J. Meeprasert, P. Maitarad, S. Nammuangruk, L. Shi and D. Zhang, *J. Phys. Chem. C*, 2016, **120**, 1523-1533.
5. D. Zhang, X. Du, L. Shi and R. Gao, *Dalton Trans.*, 2012, **41**, 14455-14475.
6. X. Du, D. Zhang, L. Shi, R. Gao and J. Zhang, *J. Phys. Chem. C*, 2012, **116**, 10009-10016.
7. F. K. Choudhury, R. M. Rivero, E. Blumwald and R. Mittler, *Plant J.*, 2017, **90**, 856-867.
8. P. Wardman, *Free Rad. Bio. Med.*, 2007, 995-1022.
9. I. Kruk, *Environmental toxicology and chemistry of oxygen species*, Springer, Berlin, 1998.
10. T. Lu and T. Finkel, *Exp. Cell Res.*, 2008, **314**, 1918-1922.

11. M. Valko, M. Izakovic, M. Mazur, C. J. Rhodes and J. Telser, *Mol. Cell. Biochem.*, 2004, **266**, 37-56.
12. H.-R. Teppo, Y. Soini and P. Karihtala, *Oxid. Med. Cellular Longev.*, 2017, **2017**, 1485283.
13. M. H. Raza, S. Siraj, A. Arshad, U. Waheed, F. Aldakheel, S. Alduraywish and M. Arshad, *J. Cancer Res. Clin. Onc.*, 2017, **143**, 1789-1809.
14. S. Wang, *Dyes Pigm.*, 2008, **76**, 714-720.
15. X.-j. Yang, P.-f. Tian, X.-m. Zhang, X. Yu, T. Wu, J. Xu and Y.-f. Han, *AIChE J.*, 2015, **61**, 166-176.
16. V. K. Bajpai, M. Kamle, S. Shukla, D. K. Mahato, P. Chandra, S. K. Hwang, P. Kumar, Y. S. Huh and Y.-K. Han, *J. Food Drug Anal.*, 2018, **26**, 1201-1214.
17. K. S. Ong, Y. L. Cheow and S. M. Lee, *J. Adv. Res.*, 2017, **8**, 393-398.
18. B. Pinegin, N. Vorobjeva, M. Pashenkov and B. Chernyak, *J. Cell. Phys.*, 2018, **233**, 3745-3754.
19. I. Celardo, J. Z. Pedersen, E. Traversa and L. Ghibelli, *Nanoscale*, 2011, **3**, 1411-1420.
20. X. Wang, Y. Hu and H. Wei, *Inorg. Chem. Front.*, 2016, **3**, 41-60.
21. C. Korsvik, S. Patil, S. Seal and W. T. Self, *Chem. Comm.*, 2007, **0**, 1056-1058.
22. Y. Yang, Z. Mao, W. Huang, L. Liu, J. Li, J. Li and Q. Wu, *Sci. Rep.*, 2016, **6**, 35344.
23. P. Attri, Y. H. Kim, D. H. Park, J. H. Park, Y. J. Hong, H. S. Uhm, K.-N. Kim, A. Fridman and E. H. Choi, *Sci. Rep.*, 2015, **5**, 9332.
24. S. Y. Yao, W. Q. Xu, A. C. Johnston-Peck, F. Z. Zhao, Z. Y. Liu, S. Luo, S. D. Senanayake, A. Martínez-Arias, W. J. Liu and J. A. Rodriguez, *Phys. Chem. Chem. Phys.*, 2014, **16**, 17183-17195.
25. M. A. Rauf, M. A. Meetani and S. Hisaindee, *Desal.*, 2011, **276**, 13-27.
26. S. Matavos-Aramyan and M. Moussavi, *Int. J. Environ. Sci. Nat. Res.*, 2017, **2**, 555594.
27. S. M. Hirst, A. S. Karakoti, R. D. Tyler, N. Sriranganathan, S. Seal and C. M. Reilly, *Small*, 2009, **5**, 2848-2856.
28. J. M. Aubry, *J. Am. Chem. Soc.*, 1985, **107**, 5844-5849.
29. G. Chen, I. Roy, C. Yang and P. N. Prasad, *Chem. Rev.*, 2016, **116**, 2826-2885.
30. E. L. Clennan and A. Pace, *Tetrahedron*, 2005, **61**, 6665-6691.
31. A. Filtschew, K. Hofmann and C. Hess, *J. Phys. Chem. C*, 2016, **120**, 6694-6703.
32. Z. Wu, M. Li, J. Howe, H. M. Meyer and S. H. Overbury, *Langmuir*, 2010, **26**, 16595-16606.
33. P. Ni, X. Wei, J. Guo, X. Ye and S. Yang, *RSC Adv.*, 2015, **5**, 97512-97519.
34. E. G. Heckert, S. Seal and W. T. Self, *Environ. Sci. & Tech.*, 2008, **42**, 5014-5019.
35. S. Wang, L. Zhao, W. Wang, Y. Zhao, G. Zhang, X. Ma and J. Gong, *Nanoscale*, 2013, **5**, 5582-5588.
36. S. Deshpande, S. Patil, S. V. Kuchibhatla and S. Seal, *Appl. Phys. Lett.*, 2005, **87**, 133113.
37. B. Ravel and M. Newville, *J. Synch. Rad.*, 2005, **12**, 537-541.
38. M. V. Piechowski, M.-A. Thelen, J. Hoigné and R. E. Bühler, *Ber. Bunsenges. Phys. Chem.*, 1992, **96**, 1448-1454.
39. T. Das, J. D. Nicholas, B. W. Sheldon and Y. Qi, *Phys. Chem. Chem. Phys.*, 2018, **20**, 15293-15299.
40. H.-X. Mai, L.-D. Sun, Y.-W. Zhang, R. Si, W. Feng, H.-P. Zhang, H.-C. Liu and C.-H. Yan, *J. Phys. Chem. B*, 2005, **109**, 24380-24385.
41. Y. Lee, G. He, A. J. Akey, R. Si, M. Flytzani-Stephanopoulos and I. P. Herman, *J. Am. Chem. Soc.*, 2011, **133**, 12952-12955.
42. L. Li, F. Chen, J.-Q. Lu and M.-F. Luo, *J. Phys. Chem. A*, 2011, **115**, 7972-7977.
43. T.-S. Wu, Y. Zhou, R. F. Sabirianov, W.-N. Mei, Y.-L. Soo and B. C. L. Cheung, *Chem. Comm.*, 2016, **52**, 5003-5006.
44. Z. M. Abou-Gamra, *Adv. Chem. Eng. Sci.*, 2014, **4**, 285-291.
45. C. A. Cohn, C. E. Pedigo, S. N. Hylton, S. R. Simon and M. A. Schoonen, *Geochem. Trans.*, 2009, **10**, 8.
46. J. J. Hu, N.-K. Wong, S. Ye, X. Chen, M.-Y. Lu, A. Q. Zhao, Y. Guo, A. C.-H. Ma, A. Y.-H. Leung, J. Shen and D. Yang, *J. Am. Chem. Soc.*, 2015, **137**, 6837-6843.
47. A. I. Cederbaum, A. Qureshi and G. Cohen, *Biochem. Pharmacol.*, 1983, **32**, 3517-3524.
48. M. E. Davis and R. J. Davis, *Fundamentals of Chemical Reaction Engineering*, McGraw Hill, New York, NY, 2003.
49. R. Zhang, J. F. Li and D. Viehland, *Comp. Mater. Sci.*, 2004, **29**, 67-75.
50. F. Voll, F. Palú and J. Santos, *Lat. Am. App. Res.*, 2011, **41**, 305-310.
51. T. A. Vetter and D. P. Colombo, *J. Chem. Ed.*, 2003, **80**, 788.
52. A. Plauck, E. E. Stangland, J. A. Dumesic and M. Mavrikakis, *Proc. Nat. Acad. Sci. U.S.A.*, 2016, **113**, E1973-E1982.
53. G. Pulido-Reyes, I. Rodea-Palomares, S. Das, T. S. Sakthivel, F. Leganes, R. Rosal, S. Seal and F. Fernández-Piñas, *Sci. Rep.*, 2015, **5**, 15613.

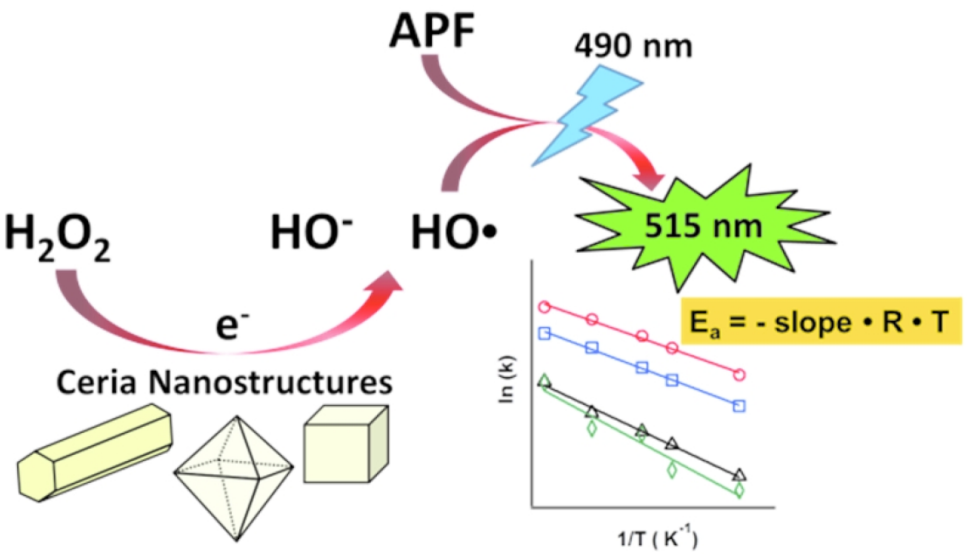

69x39mm (600 x 600 DPI)